J. Fluid Mech. (1996), *vol.* 317, *pp.* 215–239

Dynamics of a vortex ring in a rotating fluid

By R. VERZICCO[1], P. ORLANDI[1], A. H. M. EISENGA[2], G. J. F. VAN HEIJST[2] AND G. F. CARNEVALE[3]

[1]Università di Roma "La Sapienza" Dipartimento di Meccanica e Aeronautica, via Eudossiana n° 18 00184, Roma, Italy

[2] Fluid Dynamics Laboratory, Eindhoven University of Technology, PO Box 513, 5600 MB Eindhoven, The Netherlands.

[3] Scripps Institution of Oceanography, University of California, San Diego, La Jolla, CA 92093 USA.

(Received 12 September 1995 and in revised form 2 February 1996)

The formation and the evolution of axisymmetric vortex rings in a uniformly rotating fluid, with the rotation axis orthogonal to the ring vorticity, have been investigated by numerical and laboratory experiments. The flow dynamics turned out to be strongly affected by the presence of the rotation. In particular, as the background rotation increases, the translation velocity of the ring decreases, a structure with opposite circulation forms ahead of the ring and an intense axial vortex is generated on the axis of symmetry in the tail of the ring. The occurrence of these structures has been explained by the presence of a self-induced swirl flow and by inspection of the extra terms in the Navier–Stokes equations due to rotation. Although in the present case the swirl was generated by the vortex ring itself, these results are in agreement with those of Virk *et al.* (1994) for polarized vortex rings, in which the swirl flow was initially assigned as a 'degree of polarization'.

If the rotation rate is further increased beyond a certain value, the flow starts to be dominated by Coriolis forces. In this flow regime, the impulse imparted to the fluid no longer generates a vortex ring, but rather it excites inertial waves allowing the flow to radiate energy. Evidence of this phenomenon is shown.

Finally, some three-dimensional numerical results are discussed in order to justify some asymmetries observed in flow visualizations.

1. Introduction

A wide variety of flows of technical or geophysical interest involve the presence of swirl or rotation. Swirling flows of combustion chambers and cyclone separators are only two examples among many. Also, large-scale flows on our rotating planet are, to a larger or smaller extent, affected by background rotation. In the ocean, for example, convection-driven turbulent plumes show a complicated behaviour, in which one or more aligned vortices may be observed (see e.g. Ayotte & Fernando 1994).

All these flows, however, are generally quite complex owing to a number of factors, like stratification, buoyancy, etc., intervening in the motion; therefore the study of such flows is difficult. In contrast, when a single coherent structure is subject to only one of the above-mentioned factors, it can be studied in detail and many insights on complex flows can be obtained.

A jet or a plume can be thought of as an array of vortex rings that by their

interaction determine the dynamics of the whole flow. This observation motivated us to consider the motion of a single vortex ring subject to background rotation. Besides, a number of studies about the effect of a background rotation on coherent structures, oriented so that the system vorticity is parallel or antiparallel to the mean vorticity, are available in the literature (e.g. Tritton 1992; Métais *et al.* 1995). In contrast, much less analysis has been performed when the system vorticity is *orthogonal* to the mean vorticity, and the flow considered in this study belongs to this configuration.

The motion of vortex rings has attracted a great deal of attention because, even though the structure of the ring is simple, its dynamics is complex. The formation and the evolution of vortex rings are interesting *per se*; however, understanding their dynamics also helps in unravelling more complex flows such as round jets.

Vortex rings without azimuthal flow have been studied extensively. In contrast, very few works are available on vortex rings with swirl. The studies by Moffatt (1988) and Turkington (1989) were focused on finding steady solutions of the Euler equations, without investigating whether or not vortex rings with swirl were stable. Virk, Melander & Hussain (1994) focused more on the dynamics of vortex rings with helical vortex lines, showing that the presence of an azimuthal flow, regardless of how it is created, slows down the translation of the vortex ring. They provided evidence that a secondary vortex structure, oppositely signed with respect to the primary vortex, is created ahead of the ring. In that paper, however, the vortex ring was initially assigned with a prescribed azimuthal vorticity profile and circular cross-section; the azimuthal flow was then imposed by specifying the 'degree of polarization'. Although very interesting, this initial condition is very difficult, if not impossible, to create in a laboratory experiment; in contrast the vortex ring in a rotating fluid is relatively simple to produce experimentally and, in our opinion, closer to practical applications.

The aim of the present work is to investigate, by direct numerical simulations and laboratory experiments, how the presence of a background rotation affects the formation and the evolution of vortex rings generated by pushing a finite amount of fluid through a sharp-edged circular orifice. In this case, both azimuthal vorticity and velocity profiles result from the interaction between the roll-up of the thin vorticity layer released at the orifice-edge and the solid-body rotation. The result is that the vortex rings have swirl self-generated by the flow dynamics. Results have shown that the ring behaviour with respect to the rotation can be essentially divided into two regimes: 'low' and 'high' rotation. In the former the vortex ring forms in the same way as it forms without background rotation, and the induced azimuthal motion only causes minor changes in the ring dynamics. As the rotation rate increases, the changes become more pronounced until the effects of the rotation dominate the flow. It will be shown that in the 'high' rotation regime the vortex ring hardly forms, and the energy of the flow is radiated away through inertial waves. An explanation for this behaviour is given.

Finally in laboratory experiments the flow was sometimes observed to depart from axisymmetry. Three-dimensional numerical simulations have shown that this was due to a possible small initial misalignment between the axis of rotation and the direction of translation of the ring.

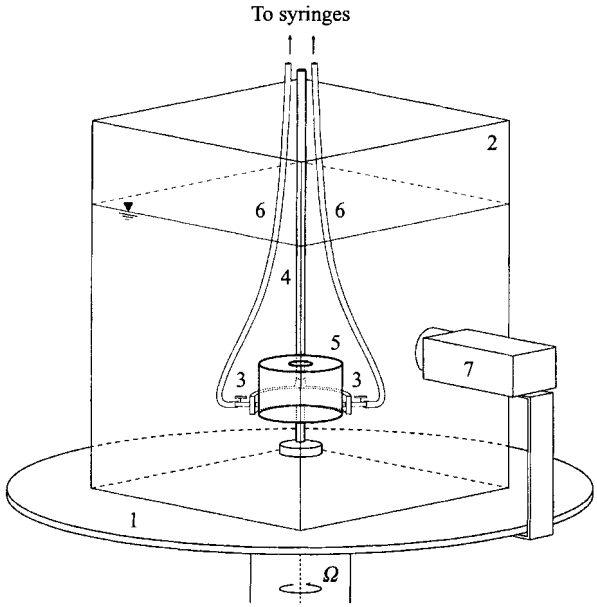

FIGURE 1. Sketch of the experimental apparatus: 1, rotating table; 2, glass tank; 3, fork; 4, stand; 5, cylindrical perspex box with the circular orifice on the top and taps in the lateral surface; 6, plastic tubes connected to the syringes driven by the step–motor system; 7, video camera.

2. Experimental set-up

2.1. *Description of experimental apparatus*

In the laboratory experiments, vortex rings were created by pushing a finite amount of fluid through a sharp-edged circular orifice cut in a thin plate. This plate was the lid of a cylindrical box (henceforth referred to as the vortex generator) with a closed bottom. The vortex generator was placed on the bottom of a large experimental tank, oriented so that all rings were fired vertically upwards. Fluid was injected into the cylindrical can from two water taps connected by reinforced plastic tubes to a set-up which could depress simultaneously up to 8 syringes by a stepmotor-driven traversing system. In this system the volume of fluid injected is controlled by the choice of the syringes used, and by the displacement of their pistons.

The vortex ring generator was placed in a glass tank of horizontal dimensions 60×60 cm and 100 cm height. This tank was put on a rotating table, whose angular velocity could be varied between $\Omega = 0.1\ \mathrm{s}^{-1}$ and $\Omega = 1.0\ \mathrm{s}^{-1}$. The vortex ring generator was positioned in such a way that the axis of rotation of the rotating table coincided with the centreline of the orifice in the ring generator (figure 1).

We have used two identical slide projectors to illuminate the vortex ring. A light sheet was created by cutting a small slit in a black slide and focusing the slide projectors. The projectors were mounted at some distance above the experimental set-up and directed downwards in such a way that the vertical light sheet crossed the centre of the orifice in the ring generator. A video camera fixed on the rotating table was used to record the experiments from the side.

The amount and the velocity of the injected fluid was controlled by the stepmotor-driven traversing system which pushed the piston of the syringes. If the pistons of N syringes are displaced by a distance L_s with a mean velocity $\overline{U}_s$, an equivalent column of fluid of length L_o is pushed through the orifice with mean velocity U. On

account of the incompressibility of the fluid, we obtained the following relationships between these parameters:

$$L_o = NL_s\left(\frac{D_s}{D_o}\right)^2, \quad U = N\overline{U}_s\left(\frac{D_s}{D_o}\right)^2, \tag{2.1}$$

where D_s and D_o denote the diameter of each syringe and of the orifice, respectively.

In our experiments we used 4, 6 or 8 syringes with $D_s = 2.5$ cm and orifices with $D_o = 3, 4$ or 5 cm. Typical values for L_s and $\overline{U}_s$ were $L_s = 1.0$ cm and $\overline{U}_s = 1.0\ \mathrm{cm\,s^{-1}}$ and these values were used for the most of the experiments.

2.2. *Experiments and data processing*

Two types of experiments, flow visualization and particle tracking, have been performed. In the first case fluorescein dye was used to visualize the vortex ring. For these experiments the water in the vortex generator was slightly dyed. The orifice of the generator was closed by an aluminium plate to avoid mixing during filling of the main tank with clear tap water. After the water tank was filled to a prescribed height and the fluid was at rest, before starting the experiment, the plate was carefully removed by pulling a wire, which was guided outside the tank by some pulleys.

Dye visualization experiments were performed to obtain a qualitative picture of the flow field of the vortex ring. The effects of background rotation on the structure and dynamics of the vortex ring were very clear and dye visualization was very helpful to interpret the observed phenomena. Also some quantitative information, including the self-induced velocity and the dimensions of the vortex ring, was gathered from this type of experiment.

In the second type of experiment, small passive tracer particles were used to determine the flow field in and around the vortex ring. We used both 100 μm and 250 μm particles, with specific weight (according to the static specification) of $\rho = 1.0 \pm 0.02\ \mathrm{g\,cm^{-3}}$. In spite of the small difference in density compared to the density of tap water the particles sank to the bottom in a relative short time (approximately 15 minutes). In order to avoid this sinking we increased the density of the fluid in the tank and vortex generator up to $\rho = 1.0325\ \mathrm{g\,cm^{-3}}$ using ordinary kitchen-salt. Now the particles floated for a longer time, typically 1–2 hours, long enough for our experiments.

The paths of the particles, which were assumed to follow the local flow field, were determined with the DigImage particle tracking technique developed by Dalziel (1992). From these particle paths the instantaneous velocity field at the position of the particles was derived. For subsequent analysis of the flow field, a spline interpolation was adapted to obtain the velocity field on a rectangular grid. Analytical differentiation of these expressions using the spline coefficients yielded the vorticity field.

3. Numerical set-up

3.1. *Equations and numerical scheme*

The time-dependent Navier–Stokes equations, written in terms of velocity and pressure, for an incompressible viscous fluid have been integrated numerically. The fluid in which the flow evolves is subjected to a solid-body rotation, with the rotation vector $\boldsymbol{\Omega} = \Omega \boldsymbol{k}$, $\boldsymbol{k}$ being the unit axial vector and Ω the rotation rate. The relative

flow in the rotating system satisfies the Navier–Stokes and continuity equations:

$$\left.\begin{aligned} \frac{\mathrm{D}\boldsymbol{u}}{\mathrm{D}t} &= -\nabla p - \frac{1}{Ro}\boldsymbol{k}\times\boldsymbol{u} + \frac{1}{Re}\nabla^2\boldsymbol{u}, \\ \nabla\cdot\boldsymbol{u} &= 0, \end{aligned}\right\} \tag{3.1}$$

with $\mathrm{D}/\mathrm{D}t \equiv \partial/\partial t + \boldsymbol{u}\cdot\nabla$ the material derivative. The equations have been non-dimensionalized by choosing suitable velocity ($\mathscr{U}$) and length (L) scales, to be specified later. The Reynolds and Rossby numbers are then defined as $Re = \mathscr{U}L/\nu$, $Ro = \mathscr{U}/2\Omega L$, where ν is the kinematic viscosity.

In order to obtain a closer comparison between flow visualizations and numerical experiments, we also simulated the evolution of a passive scalar. The equation for the scalar concentration field T is

$$\frac{\mathrm{D}T}{\mathrm{D}t} = \frac{1}{ReSc}\nabla^2 T, \tag{3.2}$$

where Sc is the Schmidt number, defined as the ratio between the kinematic viscosity ν and the scalar diffusivity κ.

The equations have been written in a cylindrical coordinate system, with the axial direction aligned with $\boldsymbol{k}$, and discretized by second-order finite-difference schemes on a staggered grid. Details of the numerical method are given in other papers (Verzicco & Orlandi 1995, 1996) and only the main features are summarized here. In the three-dimensional case, in the limit of $\nu \to 0$, the energy is conserved and this holds in the discretized equations. The system of equations is solved by a fractional-step method with the viscous terms computed implicitly and the convective terms explicitly; the large sparse matrix resulting from the implicit terms is inverted by an approximate factorization technique. At each time step the momentum equations are provisionally advanced using the pressure at the previous time step, giving an intermediate non-solenoidal velocity field. A scalar quantity Φ is then introduced to project the non-solenoidal field onto a solenoidal one. The large band matrix associated with the elliptic equation for Φ is reduced to a tridiagonal matrix using trigonometric expansions (cosFFTs) in the axial direction. The pressure is related to the scalar Φ. The third-order Runge–Kutta scheme, described by Verzicco & Orlandi (1996), is used to advance the equations in time.

Finally, in cylindrical coordinates the equations are singular at $r = 0$. The advantage of using staggered quantities is that only the radial component of the momentum equation needs to be evolved at the centreline ($r = 0$), and for this component we calculate the evolution of $q_r = ru_r$ instead of u_r since the former quantity clearly vanishes on the centreline.

3.2. *Run parameters and convergence checks*

There are many quantities that are usually chosen to render the evolution equations non-dimensional. For vortex rings it is common to take the toroidal radius and the self-induced translation velocity as length scale and velocity scale, respectively. When the background rotation is added, however, depending on the magnitude of the rotation, the characteristics of the vortex ring change, and it will be shown that, for the highest rotation rates, the vortex ring does not form at all. In these cases the above quantities are not defined and the meaning of the non-dimensional parameters becomes unclear. The same problem is encountered if the circulation of the vortex ring is used instead of the self-induced velocity. Within this scenario, it is more convenient to use quantities related to the vortex ring generator. Although these

geometric parameters are only indirectly related to the final vortex structure, on the other hand, they are always well defined. In the present case, the radius of the orifice ($R = D_o/2$) from which the fluid is ejected and the centreline ejection velocity (U) have been chosen as length and velocity scales, giving the following definitions for the non-dimensional parameters: $Re = UR/\nu$ and $Ro = U/2\Omega R$.

Once the scaling quantities are fixed, the run parameters can also be defined. The simulations have been performed in an axisymmetric domain of $R_f = 5R$ and $L_f = 8R$ in the radial (r) and axial (z) directions, respectively. The spatial discretization was uniform in z with $\Delta z = 0.031R$ while a non-uniform grid was used in r to achieve a fine resolution close to the edge of the orifice, where a thin vorticity layer rolls up initially. A coarser grid was used near the external cylindrical boundary in order to minimize the number of grid points in a dynamically passive region. The analytical transformation for the radial coordinate is

$$r = R_f r_1(\eta) * r_2(\eta), \tag{3.3}$$

with

$$r_1(\eta) = R_m/R_f \tanh(\beta\eta)\tanh(\beta\eta_m),$$

$$r_2(\eta) = \frac{1}{r_1(1)} + \left(1 - \frac{1}{r_1(1)}\right)\tanh(\alpha(\eta - 1))\tanh(\alpha(\eta_m - 1))$$

where η is the radial computational variable uniformly spaced between 0 and 1. By using the values $R_f = 5$, $R_m = 1$, $\eta_m = 0.39$, $\alpha = \beta = 3$, and 129 grid points we obtained a grid spacing of $\Delta r = 0.024R$ near the axis, $\Delta r = 0.017R$ near the orifice edge and $\Delta r = 0.1R$ in the region of the external boundary where a free-slip boundary condition has been imposed.

The time integration of the equations was performed with a constant time step $\Delta t = 0.02R/U$ which yielded a value of the stability parameter (CFL) always below unity.

Since the formation and the evolution of a vortex ring is a 'space developing flow' (i.e. a flow with the streamwise direction that is not a homogeneity direction), inflow and outflow boundary conditions have to be assigned in the axial direction. At the inlet ($z = 0$), for $0 \leqslant r \leqslant R$ we prescribed an axial velocity profile $U_z(r)$ modulated by a time dependence $f(t)$ in such a way as to reproduce the injection of fluid through the nozzle of the experimental apparatus. $U_z(r)$ is specified by

$$U_z(r) = U\frac{\tanh[(R - r)/\delta]}{\tanh[R/\delta]} \tag{3.4}$$

where δ is the initial vorticity thickness of the inflow velocity profile and we have used $\delta = R/20$ †. The function $f(t)$ starts at 0 and grows to unity by a cubic law in a time $t = 0.1R/U$, then it is constant and equal to 1 for a time $t = R/U$ and finally it goes back to zero in a time $t = 0.1R/U$. Thus the total injection time is $\mathscr{T} = 1.2R/U$, which corresponds to a dimensional time (t') of one second, according to the dimensional values of R and U used in the experiments (see §4.1). For $z = 0$ and $R < r \leqslant R_f$ all velocity components are set to zero. Identical inflow conditions have been used for the passive scalar concentration T to simulate the flow visualizations in which dyed fluid is injected from the nozzle.

Boundary conditions at the outlet are very important in space-developing flows. In

† In fact the exact definition of the vorticity thickness is $\delta_{\omega_\theta} \equiv [U/(\partial U_z/\partial r)]_{\max} = \delta\tanh[R/\delta]$; for values of $\delta \ll R$, however, $\tanh[\delta^{-1}R] \simeq 1$, so that $\delta_{\omega_\theta} \simeq \delta$.

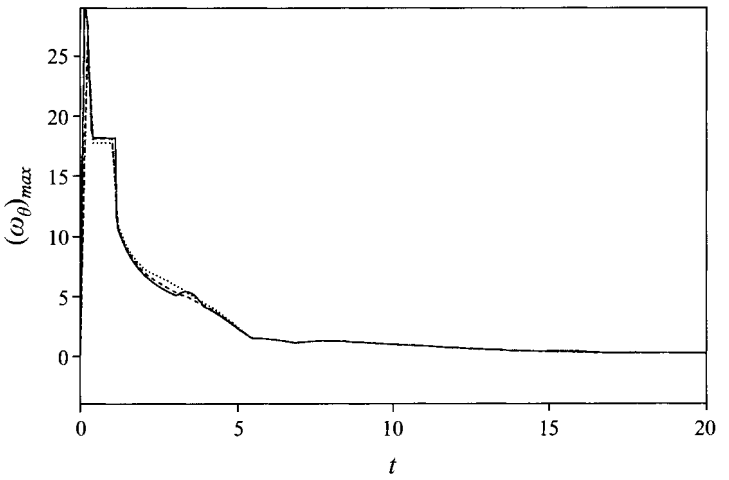

FIGURE 2. Time evolution of the maximum azimuthal vorticity for $Re = 484$ and $Ro = 1.65$: ——— 385 × 257, - - - - 257 × 129, ····· 193 × 97 grid.

our simulations, we impose that the velocity components and the passive scalar are convected out of the domain according to the relation

$$\frac{\partial Q}{\partial t} + C\frac{\partial Q}{\partial z} = 0, \tag{3.5}$$

with Q the convected quantity and C the convection velocity. In our simulations we have used the value $C = 0.6$, although it has been checked, by preliminary simulations, that the results are quite insensitive to the value of C.

All axisymmetric simulations have been performed using a grid of 257 × 129 in the axial and radial directions, respectively. The grid independence of the results has been checked by repeating one typical simulation with a coarser (193 × 97) and a finer grid (385 × 257) and comparing the results. For this comparison the run parameters were $Re = 484$ (used for almost all simulations) and $Ro = 1.65$, since we have observed that for such high rotation rates small vorticity structures are created. The comparison is shown in figure 2 for the maximum azimuthal vorticity and it looks satisfactory.

Although the hypothesis of axisymmetry was used for the most of the numerical experiments, some full three-dimensional simulations were performed (see §4.4). Owing to computer limitations, however, we were not able to achieve a satisfactory azimuthal resolution maintaining the grid of the axisymmetric cases. A good compromise was to reduce the axial and radial extension of the computational domain to $6R$ and $4R$ and the grid to 193 × 97 therefore, without changing the radial and axial spatial resolution. This solution allowed us to use 64 grid points in the azimuthal direction, which was found sufficiently fine to resolve the scales of the flow.

4. Results

4.1. *Preliminaries*

Before getting into the quantitative description of the results, it is helpful to show a couple of flow visualizations of the evolution of the vortex ring with and without background rotation, in order to appreciate the differences in the dynamics that will be studied in the successive sections.

Figure 3 shows a sequence of photographs of a dye-visualization experiment of a

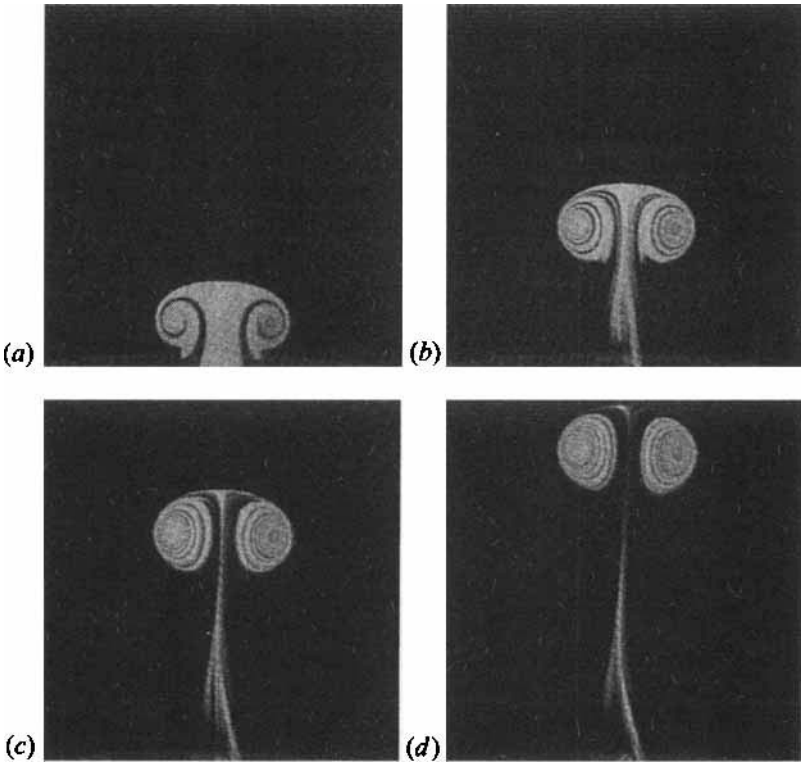

FIGURE 3. Dye visualizations of a vortex ring evolution at $Ro = \infty$ and $Re \simeq 1000$: (*a*) $t = 4$, (*b*) $t = 8$, (*c*) $t = 12$, (*d*) $t = 16$.

vortex ring, in the absence of background rotation. The orifice at which the ring was created is located just outside the bottom part of this image and is not visible here. The heights of the images in figure 3 are approximately 12 cm. A sheet of dyed fluid is rolled up in a spiral as the core of the ring forms. The spiral form of this sheet is distinguishable since undyed ambient fluid from outside the ring generator was entrained in the vortex during the formation.

As is seen in figure 3, the location and dimensions of the vortex ring are visualized by a dyed blob of fluid, which is sometimes called the vortex 'atmosphere' (Thomson 1867). This 'atmosphere' is assumed to be a closed region of fluid for steadily propagating inviscid thick rings. However, this is true only at the final stage (figure 3*d*) since initially undyed ambient fluid is entrained from the rear into the centre of the vortex ring, even after the main part of the vortex ring has been formed. Over this distance the motion of the vortex ring is laminar in all experiments, and usually the motion remains laminar even when the vortex ring moves outside the observation area, until it approaches the free surface of the water in the tank.

If a background rotation is added many additional effects arise, making the dynamics of the flow more complex. In figure 4 pictures at successive times of a dye visualization experiment of a vortex ring in a rotating fluid ($Ro = 4.8$) are shown. Initially, the vortex ring is created in the same way as in the case of no rotation. However, after the creation of the vortex ring is almost complete, a small depression is observed ahead of the vortex atmosphere (figure 4*a*). From this region a thin dye layer rolls up into a secondary vortical structure with circulation of opposite sign relative to the circulation of the primary vortex ring. This secondary vortex is

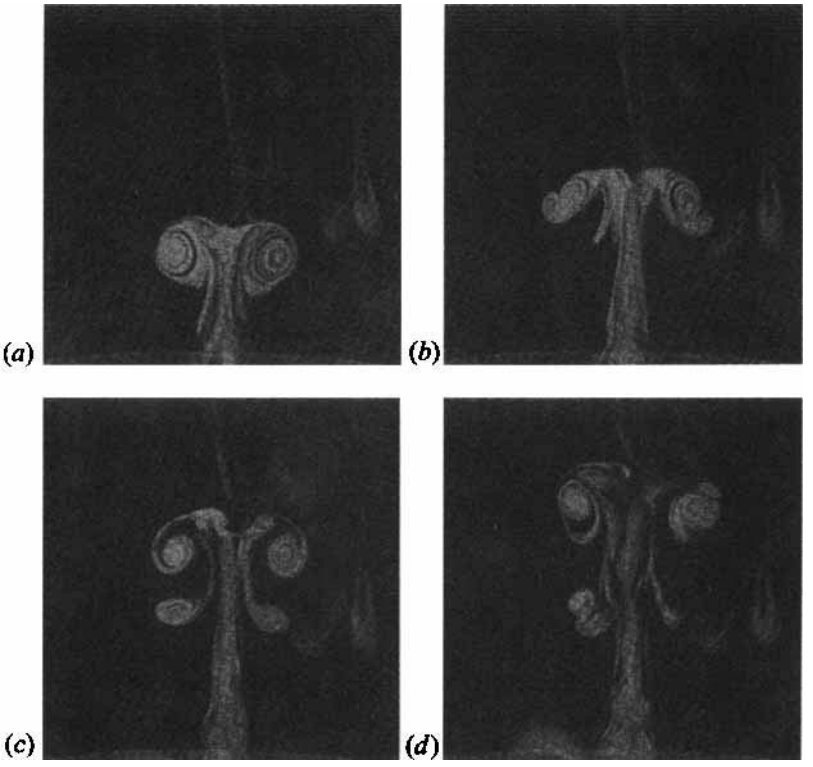

FIGURE 4. Dye visualizations of a vortex ring evolution at $Ro = 4.8$ and $Re \simeq 1000$: (*a*) $t = 7$, (*b*) $t = 10$, (*c*) $t = 13$, (*d*) $t = 16$.

then advected by the local flow field of the primary vortex ring, increasing in strength during stretching around the vortical core of the primary vortex ring (figure 4*b*). Finally, the secondary structure is completely shed from the primary vortex while its localized vorticity soon diffuses due to viscosity (figure 4*c*,*d*).

In figure 4*d* it is observed that the primary vortex ring was severely deformed during the shedding process, but it was still able to re-establish itself as a vortex ring after the shedding. Ahead of the primary ring, a third vortical structures is created in the same way the secondary vortex was formed earlier (see figure 4*a*) and the shedding process could eventually be repeated, if the primary vortex were strong enough. Usually, the viscosity weakens the vortex rings during the evolution and, after the first shedding, the primary vortex is too weak to shed a new structure. Besides now the motion loses its axisymmetry and it is less clear from a two-dimensional view how the flow field evolves three-dimensionally. In order to have a better picture of the phenomenon, and to understand the causes of this loss of symmetry, a few three-dimensional simulations have been performed and the results presented in §4.4.

Summarizing the entire process, we have seen that the first effect of the rotation is to form a depression ahead of the vortex ring. From this depression, oppositely-signed vorticity develops and eventually rolls up to generate a counter-rotating secondary vortex ring which is shed behind the primary ring. The impulse of the primary ring is reduced by shedding of secondary structure and this is evidenced by the shorter distance traveled by the ring at $t = 16$ (figure 4*d*) compared to the case without rotation (figure 3*d*). For successive times the rings can lose the axisymmetry and the flow shows complex three-dimensional structures. These features have been inferred

from flow visualizations that, if they showed the evolution of a passive scalar, might present a different behaviour. However, Orlandi & Verzicco (1993) have shown that there is a strong correlation between azimuthal vorticity and passive scalars if the flow remains axisymmetric; therefore, at least the gross features of the flow dynamics can be understood by flow visualizations.

Except for these flow visualizations, in all laboratory experiments we have used fixed generation parameters for the vortex rings: $L_s = 1$ cm, $\overline{U}_s = 1\ \mathrm{cm\,s^{-1}}$ (yielding an injection time $t' = 1$ s), $N = 6$, and an orifice diameter of $D_o = 4$ cm. This implies that an equivalent cylindrical column of fluid is injected through the orifice of length $L_o = 2.4$ cm and mean velocity $U = 2.4\ \mathrm{cm\,s^{-1}}$. For the experiments the value of Re was thus fixed at $Re = UR/\nu = 484$, with $\nu = 0.01\mathrm{cm^2\,s^{-1}}$ (the kinematic viscosity of water at ambient temperature).

In order to be able to distinguish the effects of the rotation, we summarize the main features of the evolving vortex at $Re = 484$ in the absence of rotation, which will be considered as a 'basic state'. Saffman (1975) and Sallet & Widmayer (1979) report that the formation process is completed after the ring has moved several ring radii (4–6) downstream from the generating orifice, and figure 5(*a*) shows the fully formed ring after about 5 ring radii. Its radius is $\overline{R} = 1.012R$, the translation velocity $v = 0.275U$ and the circulation $\Gamma = 1.525UR$, giving for the Reynolds numbers defined for the ring $Re_{\overline{R}} = v\overline{R}/\nu \simeq 133$ and $Re_\Gamma = \Gamma/\nu \simeq 738$. To give an idea of the thickness of the ring, we have also computed a 'speed-effective core size' a_e (Saffman 1978), namely the core size of the uniform-vorticity ring which matches the speed of the present ring. From the formula for the translation velocity of vortex rings (Kelvin 1867)

$$v = \frac{\Gamma}{4\pi\overline{R}}\left[\ln\frac{8\overline{R}}{a_e} - \frac{1}{4}\right], \tag{4.1}$$

we obtain $a_e = 0.64\overline{R}$.

Figure 5(*b*) shows a plot of the passive scalar distribution in the (r,z)-plane, obtained for $Sc = 10$. This value is certainly far from the Schmidt number of dye in liquids, which is typically $O(500$–$1000)$; owing to resolution problems, however, such values are too large for the numerical simulations. Our aim is only to partially account for the different diffusivity between vorticity and passive scalar to study its effects. We should note that even though a relatively low Schmidt number has been used for the simulations, the passive scalar in figure 5(*b*) looks slightly under-resolved. However, this is not a problem for the dynamics since the scalar is only a passively convected quantity and does not interact with the flow dynamics which, in contrast, is very well resolved. We wish also to stress that the low Schmidt number used in these simulations prevents the passive scalar field from forming spiralling patterns like those in figures 3 and 4. Verzicco & Orlandi (1995) performed simulations at $Sc = 100$ and they observed spirals like those of flow visualizations; however, in that case only the initial formation of the vortex ring was simulated and a very fine spatial discretization could be achieved. In this case, in contrast, we focus more on the evolution of the vortex ring and a larger computational domain is needed. The same spatial resolution used by Verzicco & Orlandi (1995) in such a large domain would require a large number of grid points, which is beyond our present computing capabilities.

For times larger than $17R/U$, the ring only undergoes a slow viscous decay, translating with a velocity that decreases in time ($v \simeq 0.16U$ at $t = 30R/U$) due to viscous effects. Finally by comparing the ring parameters computed above with

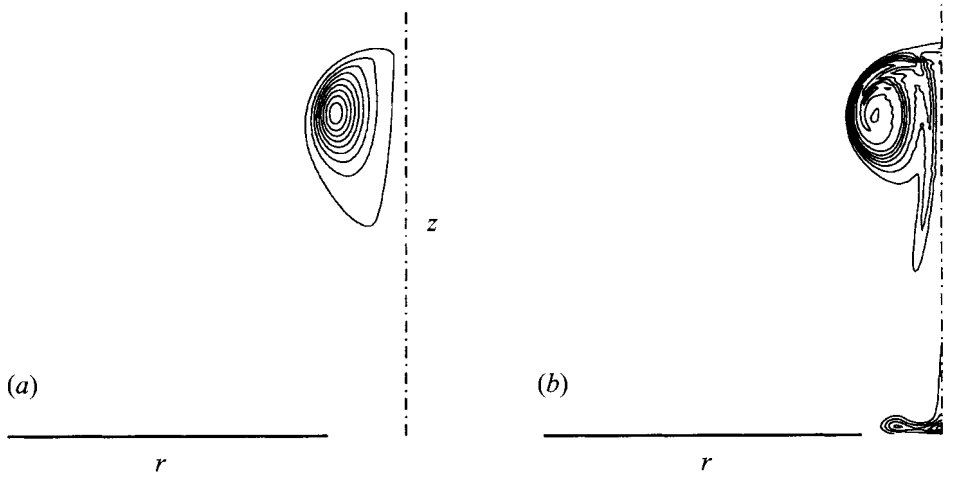

FIGURE 5. (*a*) Contour plots of azimuthal vorticity at $t = 17$, $Re = 484$ and $Ro = \infty$; $\Delta\omega_\theta = 0.2$, all values positive. (*b*) Corresponding contour plots of passive scalar at $Sc = 10$, $\Delta T = 0.1$. In this, and in all other numerical figures, the unit length is the radius of the nozzle.

data given in Shariff, Verzicco & Orlandi (1994), we find that this ring is stable to azimuthal perturbations †, and this further justifies the axisymmetric nature of most of the simulations.

In figure 4, we have seen that the evolution of the vortex ring is strongly influenced by the background rotation. Laboratory experiments and numerical simulations have shown that the flow dynamics can be roughly divided into two regimes: 'low rotation' ($Ro \gtrsim 3$) and 'high rotation'. In the former regime, the rotation constitutes only a perturbation on the basic state, while in the latter the rotation dominates the flow and the vortex ring hardly evolves or even forms. In the next subsection we will discuss the low-rotation regime, while the second regime will be addressed in § 4.3.

4.2. *Low-rotation regime*

As the ring starts moving, a layer of oppositely signed azimuthal vorticity forms ahead of the primary ring and this tends to slow down the vortex. In fact, without the secondary structure, any cross-section of the primary ring is moving because it is being convected by all of the other sections of the ring of circulation Γ. When the counter-rotating secondary vortex is formed there is a loss of effective circulation, being the sum of the circulations of both rings. In other words, the motion of each cross-section of the ring is slower because the presence of the secondary ring in effect reduces the circulation everywhere along the ring.

† The computation of the stability parameters implies also the calculation of a, the equivalent circular core radius of the ring with the same circulation, a_1 the 'inner core radius' which maximizes the tangential velocity and ϵ one of the parameters of the confluent hypergeometric function (Abramowitz & Stegun 1964) that specifies the vorticity distribution within the core. Saffman (1978) gives the way of computing these quantities, together with an estimate of the self-induced rate of strain σ and critical Reynolds number Re_S with:

$$\sigma = \frac{3\Gamma}{16\pi\bar{R}^2}\left[\ln\frac{8\bar{R}}{a_e} - \frac{17}{12}\right], \quad Re_S = \frac{\sigma a_1^2}{\nu}.$$

Shariff *et al.* (1994) by direct numerical simulations found the critical Re_S to be $\simeq 18$, while the present calculations are in the range $Re_S \simeq 15.5$ that is below the region of growing azimuthal instabilities.

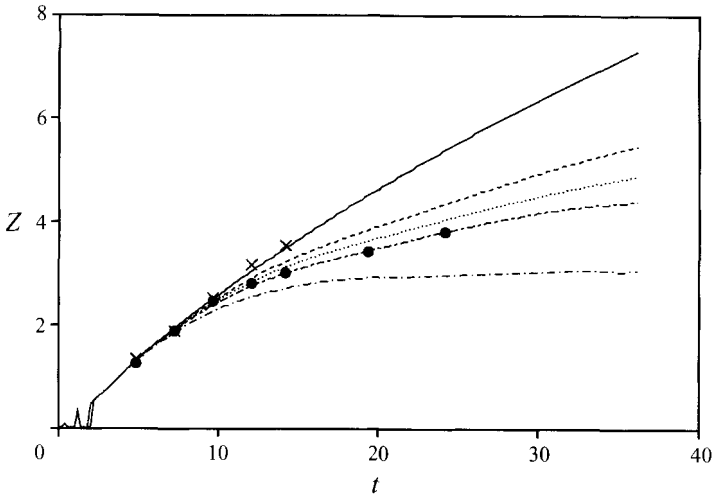

FIGURE 6. Time evolution of the axial position of the core centre of the ring (Z) for $Re = 484$ and: ——— , $Ro = \infty$; - - - - , $Ro = 10$; ····· , $Ro = 7.4$; — - — , $Ro = 5.5$; — · — , $Ro = 3$. Experimental results: × , $Ro = \infty$; • , $Ro = 5.5$.

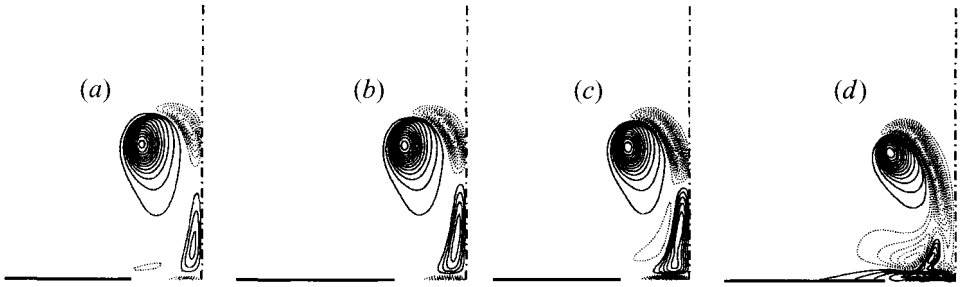

FIGURE 7. Contour plots of azimuthal vorticity at $t = 7.26$, $Re = 484$ and $Ro = 10.0$ (a), $Ro = 7.4$ (d), $Ro = 5.5$ (c) and $Ro = 3.0$, vorticity increments $\Delta\omega = \pm 0.25$. In this and subsequent similar figures, solid lines denote positive values and dotted lines negative values.

In figure 6, the time evolution of the axial coordinate of the centre of the core is shown for several values of Ro; for comparison the trajectory of the ring without rotation is given as well. Although data are presented only for $Re = 484$ the same behaviour has been observed for different Reynolds numbers that, even if changed by a factor of three, produced no changes in the trajectories comparable with those induced by rotation effects. It can be noticed that only a small part of the velocity decrease is due to the viscosity, while a larger effect is induced by the rotation. The graph also contains data plots of experimental trajectories obtained for two different cases with parameter values as in two of the numerical simulations. The agreement is very good, confirming that the numerical set-up mimics well the laboratory experiments.

Figure 7 presents some azimuthal vorticity contour plots for the cases shown in figure 6. It appears that as the Rossby number decreases, the oppositely-signed structure, inferred from flow visualizations, strengthens, and thus causes a deceleration of the primary ring. The same phenomena have been observed by particle tracking experiments, and figure 8 shows one typical observation. From the particle paths of figure 8(a) the velocity field is computed (figure 8b) and this field is interpolated on

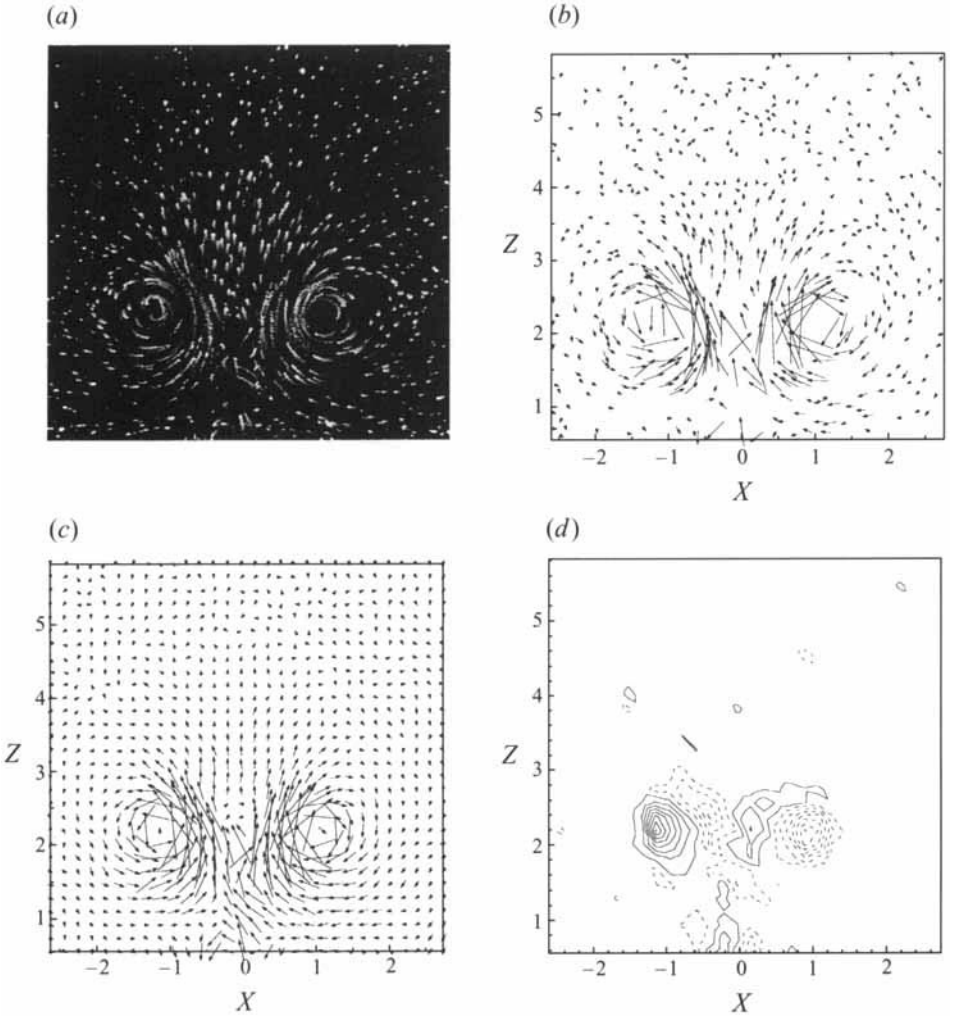

FIGURE 8. Particle trajectories (*a*), measured velocity (*b*), interpolated velocity (*c*) and azimuthal vorticity (*d*), of a vortex ring at $Ro = 3.5$ and $Re = 484$ and $t = 6$. Vorticity increments $\Delta\omega = 0.5$.

a regular grid by splines (figure 8*c*) to compute finally the azimuthal vorticity field (figure 8*d*). Although the vorticity shows some low-level noise, the secondary structure ahead of the primary ring is clearly discernible. Also note in figure 8(*d*) the vorticity in the tail, which was completely absent in the flow without background rotation.

A simple explanation for the appearance of these additional vorticity structures is obtained by inspection of the azimuthal vorticity transport equation in the presence of background rotation:

$$\frac{\partial \omega_\theta}{\partial t} + (\boldsymbol{u} \cdot \nabla \boldsymbol{\omega})_\theta = (\boldsymbol{\omega} \cdot \nabla \boldsymbol{u})_\theta + \frac{1}{Ro}\frac{\partial u_\theta}{\partial z} + \frac{1}{Re}(\nabla^2 \boldsymbol{\omega})_\theta, \tag{4.2}$$

where the second term at the right-hand side represents the effect of the system rotation. Axial gradients of azimuthal velocity constitute a source for azimuthal vorticity. Consider first a vortex ring without rotation, the velocity field of which is shown in figure 9; owing to the velocity tangential to the core a parcel of fluid initially located close to the axis at position A in figure 9 will be transported to a

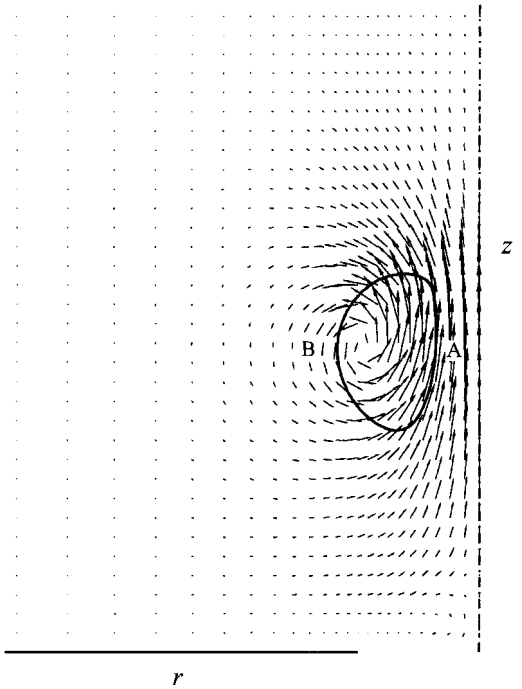

FIGURE 9. Velocity vectors and sketch of the boundary of the core of the ring for $Re = 484$ and $Ro = \infty$, the ring translates upwards. A and B are positions of parcels of fluid initially close to and far from the axis, respectively.

location farther from the axis-turning around the front of the ring. In contrast, a parcel initially far from the axis at position B in figure 9 will be convected toward the axis-turning around the rear part of the ring. Now, if we introduce the effect of the rotation, considering the conservation of the angular momentum, wherever there is an outward radial motion the azimuthal velocity has to decrease, while it has to increase where the radial motion is directed inward. This increase is illustrated by figure 10(*d*) which shows a map of azimuthal velocity for a vortex ring at $Ro = 7.4$. Evidence of the strong positive swirling motion is also given in figure 10b, which shows an intense axial vortex on the axis of symmetry that was also observed by Virk *et al.* (1994). The presence of strong positive swirl below the rising vortex structure was clearly observed in the experiments as well. The negative swirl, in contrast, is less evident and figure 10(*d*) shows that it is much weaker. This is not surprising, since by the conservation of the angular momentum, a radially displaced parcel of fluid has to preserve the quantity $(ru_\theta + r^2\Omega)$. Thus it turns out that an inward radial motion δr, with respect to an initial position r_0, will be accompanied by an increase of the azimuthal velocity that is larger than the corresponding decrease due to the same displacement δr performed radially outward.

If one moves along a line parallel to the axis and passing through the maximum of u_θ ($r \simeq 0.25$ in figure 10*d*), one first encounters a positive axial gradient of azimuthal velocity ($\partial u_\theta/\partial z > 0$), whereas further up it becomes negative. According to equation (4.2), this implies a region of positive azimuthal vorticity generation close to the axis and in the rear part of the ring, while in the front there is a region of negative azimuthal vorticity generation, consistent with the flow map of figure 10(*a*). For completeness, in figure 10(*c*) the radial vorticity component is also reported, which

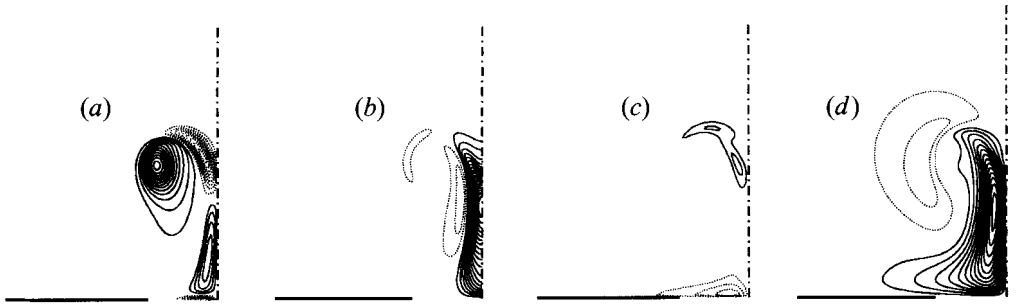

FIGURE 10. Contour plots of ω_θ (*a*), ω_z (*b*), ω_r (*c*) and u_θ (*d*), at $t = 7.26$ for $Re = 484$ and $Ro = 7.4$. Vorticity increments $\Delta\omega = \pm 0.25$, velocity increments $\Delta v = \pm 0.02$.

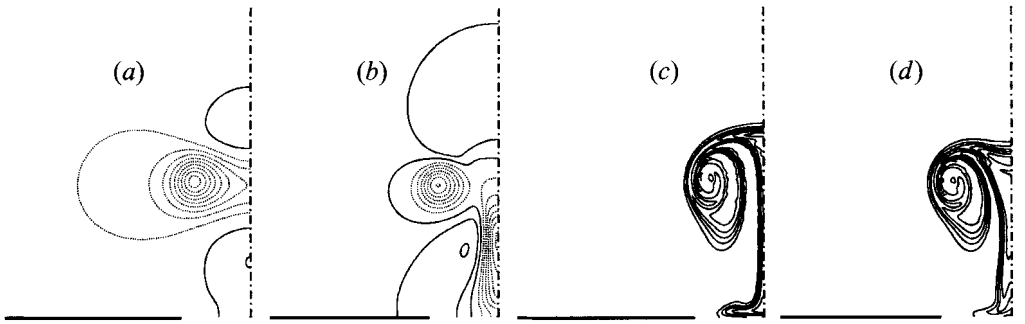

FIGURE 11. Contour plots of pressure (*a,b*) and passive scalar (*c,d*) at $t = 7.26$, $Re = 484$ and $Sc = 10$: (*a,c*) $Ro = \infty$, (*b,d*) $Ro = 5.5$. $\Delta T = 0.2$, $\Delta p = 0.015$.

remains always small in magnitude and does not contribute significantly to the flow dynamics.

Note that the presence of some azimuthal motion like that of figure 10(*d*) is consistent with the decreased translation velocity of the ring according to the arguments of Virk *et al.* (1994, formula 33).

An alternative way of explaining the deceleration of the ring is obtained by considering the behaviour of the pressure due to the presence of an anticyclone in front of the ring and a cyclone at its rear. Since pressure is lower in cyclones than in anticyclones, during the motion the ring has to counteract the effect of an adverse pressure gradient which exerts on the ring a force opposite to the direction of translation. That the pressure effectively behaves as described above has been verified by looking at its distribution for a vortex ring both in the absence of background rotation ($Ro = \infty$) and for the case at $Ro = 5.5$ (figure 11*a,b*). The corresponding passive scalar distributions are shown in figure 11*c,d*. In the former case the front of the ring is concave according to the classical picture given in many studies; in contrast, in the case with rotation the head of the ring shows the depression, already shown in flow visualizations, that is due to the pressure being higher at the front than at the rear.

As the evolution of the ring proceeds, the interaction with the oppositely signed structure continues, and this has two main effects: the first is an outward radial motion of the ring; the second is a decrease of the peak vorticity due to cross-cancellation (viscous diffusion of both vorticity maxima). The first effect is easily explained if the coupled ring plus secondary structure is thought of as an 'unbalanced dipole', that would move radially outward along a curvilinear path since the positive lobe

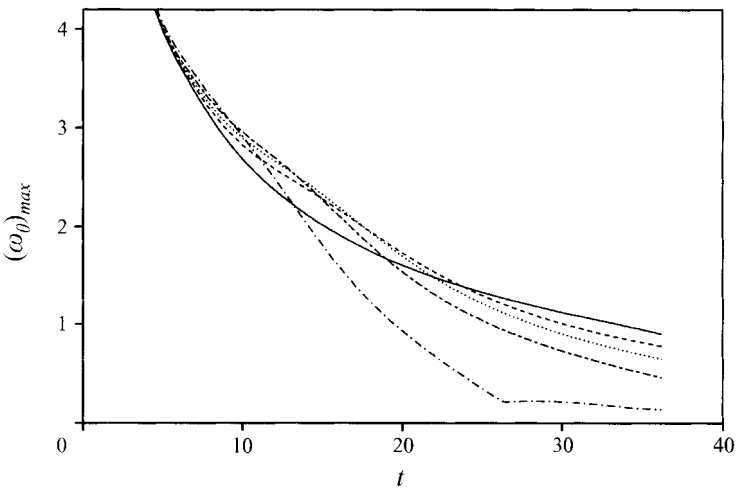

FIGURE 12. Time evolution of the maximum azimuthal vorticity for $Re = 484$ and ——— , $Ro = \infty$; - - - - , $Ro = 10$; ····· , $Ro = 7.4$; — - — , $Ro = 5.5$; — · — , $Ro = 3$.

is stronger than the negative. Looking at equation (4.1) this outward radial motion could be used as a further argument to interpret the slowing down of the ring. In fact the flow is not two-dimensional and the positive radial motion is accompanied by an increase of the vorticity and a reduction of the cross-sections because of vortex stretching. This mechanism increases vorticity gradients considerably and enhances the diffusion, until for higher rotations the ring almost disappears completely. Evidence of this behaviour is given in figure 12 where the time evolution of the peak vorticity of the ring is shown for several rotation rates; again the curve for $Ro = \infty$ is included for comparison. For early times $t \leqslant 5$, the peaks all have the same value because the secondary structure is still too weak to influence the core of the ring, but later the outward radial motion becomes evident and the peak vorticities increase, compared to the case at $Ro = \infty$, due to stretching. Of course, with the stretching, vorticity gradients are also augmented, and the increase of vorticity is followed by a rapid decrease due to diffusion. An extreme case of vorticity diffusion is represented at $Ro = 3$. In this case, the 'knee' in the curve at $t \simeq 27$ indicates that the ring has almost disappeared by $t \simeq 27$ and the peak vorticity plotted in the figure is no longer located in the ring, but rather in a structure in the tail left behind. The case at $Ro = 3$ is a limit case in which the ring is still identifiable for most of the evolution; for lower Ro the 'knee' in the curve of maximum azimuthal vorticity moves to the left of the time axis (see figure 2) meaning that the vortex ring survives for a shorter time. For values of the Rossby number lower than about 1 the effects of the rotation become dominant from the beginning, and the next subsection is devoted to the study of this regime.

All cases presented so far in this subsection have been computed using a fixed Reynolds number ($Re = 484$) since this was the value at which most of the experiments were performed. However, viscous effects play a large role in the flow dynamics and therefore it is important also to examine how the flow changes for increasing Reynolds numbers. Contour plots showing the evolution of the azimuthal vorticity for the case at $Re = 1500$ and $Ro = 10$ are displayed in figure 13. This ring evolution is essentially the same as that in the laboratory experiment shown in figure 4 where in fact the Reynolds number was $\simeq 1000$. The first part of the evolution, i.e. the formation of

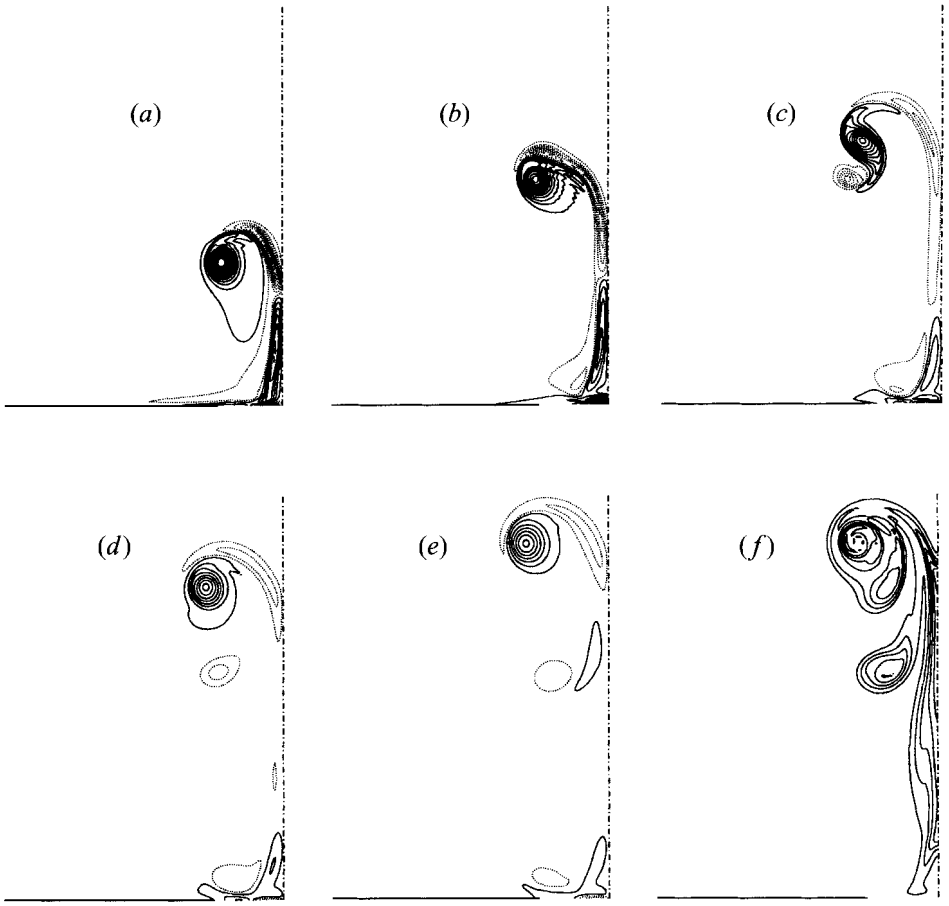

FIGURE 13. Contour plots of azimuthal vorticity at $Re = 1500$ and $Ro = 10$: (*a*) $t = 7.2$, (*b*) $t = 12.1$, (*c*) $t = 16.9$, (*d*) $t = 21.8$, (*e*) $t = 26.6$. (*f*) Contour plot of passive scalar at Sc= 3.2 and $t = 26.6$. Vorticity increments $\Delta\omega = \pm 0.5$, passive scalar increments $\Delta T = \pm 0.1$.

the oppositely signed structure, is essentially inviscid and simulations performed at different Reynolds numbers have revealed that the features of the flow are the same. However, the later stage of the evolution implies diffusion of vorticity and this is strongly dependent on viscosity. As the viscosity is decreased cross-cancellation of vorticity is prevented, and the oppositely signed vortex, instead of diffusing as in the previous case, lives long enough to be elongated by the strain field of the primary ring. During the straining process, in the interval between figures 13(*b*) and 13(*c*), the secondary vortex wraps around the primary one, becoming a thin vorticity layer that, being unstable, rolls up to form a secondary vortex moving in a direction opposite to the primary. This secondary ring should experience flow dynamics similar to that described above with the role of positive and negative vorticity reversed; however, this structure is smaller and weaker than the primary ring and is thus rapidly diffused. Also the primary ring is not strong enough to generate a new secondary ring, and so it continues its translation with a dynamics similar to that described for low Reynolds numbers.

Figure 13(*f*) shows the distribution of passive scalar at the same time as figure 13(*e*). Note that most of the scalar is entrained in the core of the primary ring, but some of it is at the location where the secondary ring is disappearing. Despite the fact that this

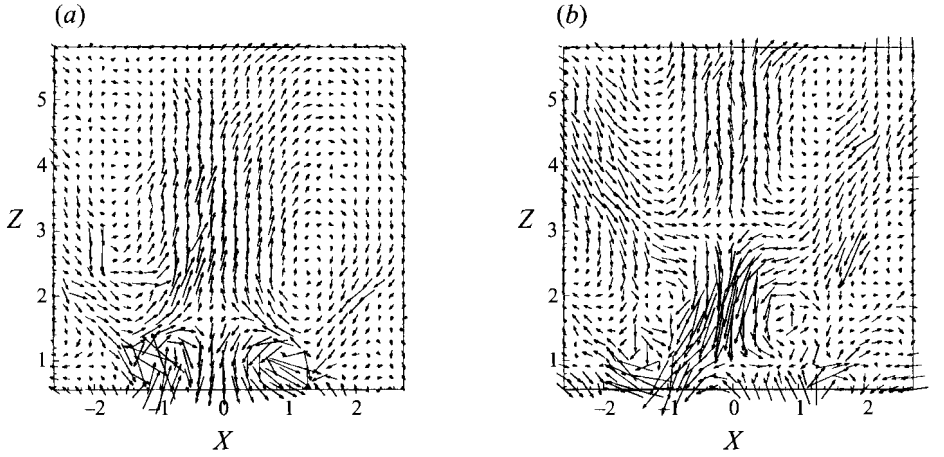

FIGURE 14. Interpolated velocity field of a laboratory vortex ring at $Ro = 0.605$ and $Re = 484$: (*a*) $t = 4$, (*b*) $t = 6$.

secondary structure has vanishing intensity, the scalar concentration almost equals that in the core of the primary ring. This is not surprising, since the scalars account for the whole history of the flow and at $t \simeq 17$ the two rings were of comparable intensity. On the other hand, this fact has to be kept in mind when quantitative conclusions are drawn from flow visualizations: regions of fluid indicated by high concentrations of dye might not have any counterpart in terms of vorticity.

4.3. *High-rotation regime*

If the Rossby number is further decreased, rotation effects no longer act as just a perturbation of the basic state, but rather they dominate the flow. Figure 14 displays a typical experimental flow pattern obtained in the same way as figure 8(*c*), but showing completely different phenomena. In particular, the initial roll-up of the shear layer is accompanied by a column of fluid pushed ahead of the ring and by oblique wave-like structures confined in thin layers (figure 14*a*).

Immediately after the forcing is stopped, the vortex ring almost disappears, and only the column and the wave structures are left in the field (figure 14*b*). In this case, the computation of the azimuthal vorticity field from the flow maps of figure 14 does not result in a clear coherent vortex structure like that shown in figure 8*d*, since in this regime the vorticity magnitude of the flow structures is too close to that of the background noise. Therefore, to better understand the vorticity dynamics, we have carried out a numerical simulation for the same experimental conditions. Figure 15 shows that immediately after the ejection, oppositely signed vorticity develops (figure 15*a*), partly due to the presence of a no-slip wall and partly, ahead of the ring, due to the mechanism described in §4.2. In this configuration, the incipient vortex is shielded by intense oppositely signed layers, and the cross-cancellation becomes dominant (figure 15*b*). Therefore, the vorticity structures weaken in time until they are completely diffused. Indirect evidence for this behaviour is also given in figure 15(*f*) where it is seen that the passive scalar ejected from the nozzle does not show any roll-up symptoms, but rather it behaves, during the whole evolution, like a two-dimensional column. Again, we observe a strong depression in the front of the column due to the high pressure generated by the strong anticyclone formed at the beginning.

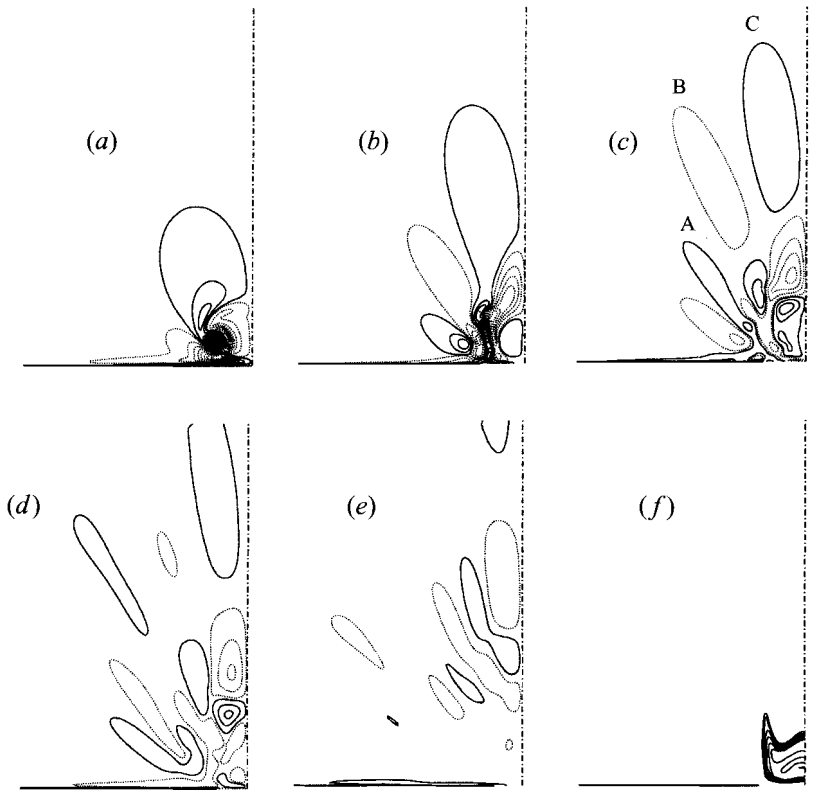

FIGURE 15. Contour plots of azimuthal vorticity at $Re = 484$ and $Ro = 0.605$: (*a*) $t = 2.4$, (*b*) $t = 4.8$, (*c*) $t = 7.2$, (*d*) $t = 9.7$, (*e*) $t = 14.5$. (*f*) Contour plot of passive scalar at Sc= 10 and $t = 14.5$. Vorticity increments $\Delta\omega = \pm 0.4$ (the minimum vorticity level is $|\omega| = \pm 0.1$ to show the oblique shear layers); passive scalar increments $\Delta T = 0.1$.

Similarly to the experiment, figure 15 shows that the high-rotation regime introduces oblique shear layers of large axial extent (like those indicated by A, B and C in figure 15*c*) that were not evident in the low-rotation regime. It is tempting to identify these structures as inertial waves which allow the ring to radiate energy, and in this case only the linear terms of the Navier–Stokes equation should be important. This eventuality has been verified by performing two simulations at $Ro = \sqrt{2}/2$, one with the nonlinear terms cancelled out. Typical results are presented in figure 16, showing that while the vorticity near the nozzle is affected by the nonlinear terms, the wave patterns are almost indistinguishable, thus proving that effects of nonlinearity are negligible in the far field.

The inertial wave radiation patterns in our simulation are somewhat complicated because the source is transient and not a simple oscillation. Greenspan (1968) shows that in the case of a single-frequency source (f^*), the inertial wave patterns are particularly simple. He considers an oscillating disk in a rotating tank. Provided that $\Omega > f^*/2$ the problem is a hyperbolic wave one in which thin free shear layers are generated at an angle with the axis of rotation $\gamma = \sin^{-1}(f^*/2\Omega)$. In our problem, in terms of the non-dimensional variables, the orientation angle γ of the wave would be

$$\gamma = \sin^{-1}(Rof) \tag{4.3}$$

with $f = f^*R/U$.

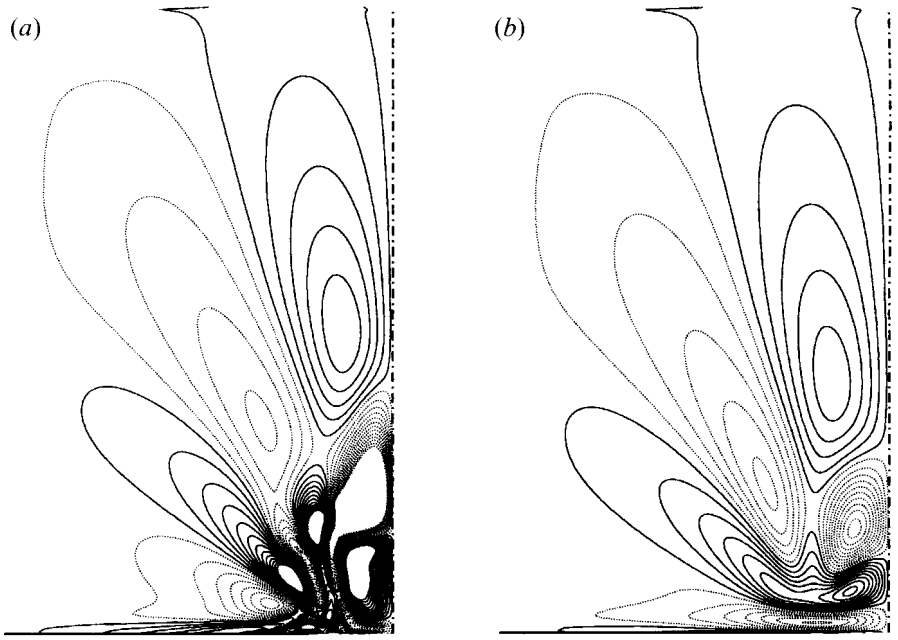

FIGURE 16. Contour plots of azimuthal vorticity at $Re = 484$, $Ro = 0.707$ and $t = 7.2$: (*a*) full Navier–Stokes run, (*b*) linear run. Vorticity increments $\Delta\omega = \pm 0.05$.

It is tempting now to use the relation (4.3) also to estimate the angles of the structures observed in the vortex ring at high rotation rates. The problem in applying (4.3) to the flow configuration of figure 15 is that there is not an obvious way to estimate f since in this problem the injection of flow is not periodic and there are many excited frequencies. What could be done however, is to focus on one structure (for example that indicated by B in figure 15*c*) and to measure its angle γ. Then from equation (4.3) it is possible to compute the corresponding frequency f_B. Since the way of injecting fluid is the same for all cases, and the Rossby number is the only parameter changing, f_B can be used to estimate the angle γ of the corresponding structures for different Rossby numbers flows. From figure 15(*c*) the inclination of the structure indicated by B is $\gamma \simeq 24.5°$, from which equation (4.3) yields $f_B = 0.685$. This value then has been used to predict the inclination of the corresponding structures formed in the flow at $Ro = 0.8$ and $Ro = 0.48$, obtaining respectively $\gamma_{0.8} = 33°$ and $\gamma_{0.48} = 19.5°$. The same angles were measured directly from the flow maps of figure 17, and this yielded $\gamma_{0.8} = 30°$ and $\gamma_{0.48} = 19°$ which are in good agreement with the estimated values. One could object that the choice of f_B is quite arbitrary since in figure 15(*c*) there is a wide range of angles from which a frequency f can be computed. The same analysis has been performed using the inclinations of the structures indicated by A and C in figure 15(*c*) and the agreement between measured and estimated values of γ for the other cases was as good as for B.

We also would like to stress that, differently from Greenspan (1968), in the case of the vortex ring the flow is forced only during the injection phase; therefore, the angle of the structures changes in time (note that the comparison between the structures of figure 15*c* with those of figure 17*a,b* has been performed at a fixed time $t = 7.2$). In particular, figure 15 shows that as time increases, the apex angle of the structures tends to diminish in the same way as observed by Stevenson (1973) for transient internal waves in a stratified fluid. In his laboratory experiments, Stevenson (1973)

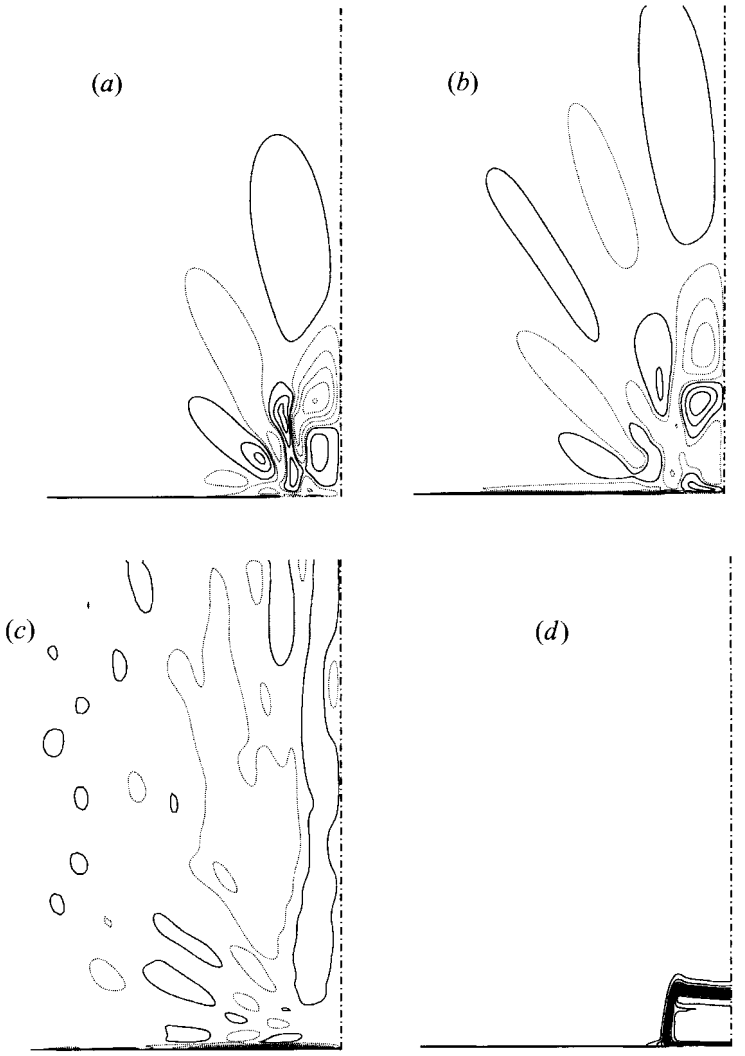

FIGURE 17. Contour plots of azimuthal vorticity at $Re = 484$ and $t = 7.2$: (*a*) $Ro = 0.8$, (*b*) $Ro = 0.48$, (*c*) $Ro = 0.1$. (*d*) Contour plot of passive scalar at $Ro = 0.1$. Vorticity increments $\Delta\omega = \pm 0.4$, (the minimum vorticity level is $|\omega| = \pm 0.1$ to show the oblique shear layers), passive scalar increments $\Delta T = 0.1$.

demonstrated that the angle of the internal waves created by an oscillating cylinder tends to decrease down to zero when the forcing stops.

Finally we also tested the limit of very high rotation rates by performing a simulation at $Ro = 0.1$. In this case the predicted angle for the 'B' type structures is only 5°, indicating that the shear layers then tend to be almost axially directed and the whole flow becomes two-dimensional. Alternatively, if in (4.2) we take the limit of $Ro \to 0$ we obtain $\partial u_\theta / \partial z = 0$; this is exactly the Taylor–Proudman theorem, predicting a two-dimensional motion independent of the axial coordinate. In fact, figure 17(*c*) shows the azimuthal vorticity field with very weak shear layers approximately parallel to the axial direction, in agreement with the predictions of the theory. Evidence of the two-dimensionality of the flow in this regime is also obtained from the passive scalar, now distributed in a column as shown in figure 17(*d*).

4.4. *Three-dimensional results*

The final point that we address is the loss of axial symmetry observed in some of the laboratory experiments (see figure 4*d*). In these cases it appeared that the ring developed an asymmetry which led one side of the ring to evolve faster than the other, yielding a translation of the ring with a certain angle with respect to the axis of rotation. In particular, it was observed that when the Reynolds number of the flow was low the inclination remained small and the flow maintained its axisymmetry. In contrast, for higher Reynolds numbers the inclination amplified in time and the flow degenerated to a fully three-dimensional configuration, as shown in figure 4.

One possible explanation was the appearance of a Widnall instability. In the experiments, however, the evolution of the ring did not show the classical wavy signature with azimuthal wavenumber n, but rather an asymmetric mode with $n = 1$. To further test this point, we performed a three-dimensional simulation with an azimuthally corrugated nozzle in such a way to excite the first 16 azimuthal modes of the ring. After the ring formation, the energy of all azimuthal modes decayed in time confirming that a Widnall type instability is not excited even with background rotation.

A second possibility is that the ring may have come out of the nozzle slightly unbalanced due to asymmetries in the generating device. This was tested in numerical simulations by letting the vorticity thickness (cf. equation (3.4)) be a function of the azimuthal coordinate $\delta(\theta) = R/(20 + \epsilon \cos\theta)$. Using values of ϵ up to 9 we were able to achieve differences between the vorticity peaks at $\theta = 0$ and $\theta = \pi$ of up to 30% without observing any significant deviation of the direction of translation from the axial direction. This might seem very surprising, since one would expect that the most intense section of the ring ($\theta = 0$) would induce the largest velocity on the weak part ($\theta = \pi$) leading to a curved path of the ring with the centre of rotation in the plane $\theta = 0$. The interpretation of the vorticity dynamics, however, reveals that this scenario is unlikely since vorticity differences along the axis of a vortex tube cannot be steadily maintained, as was shown by Verzicco, Jiménez & Orlandi (1995). In analogy with that case, in the unbalanced ring the vorticity difference will produce a pressure gradient along the toroidal axis that will drive the fluid from the portion of the ring with low vorticity toward the portion with high vorticity. The consequence is that the region with weak vorticity will be stretched while the strong counterpart will be compressed, leading to a situation that is opposite to the initial one. The viscosity of the flow damps this wave and after a few oscillations it forms a uniform-core vortex ring.

Another suggestion about the occurrence of the asymmetry was that the vortex ring was initially not aligned precisely along the axis of rotation. This seems reasonable since it is difficult in the experimental set-up to detect angles of the order of $2 - 3^\circ$ and a small deviation yields an angle between the direction of propagation and the direction of the rotation vector. Suppose that the rotation vector forms an angle ε with the axial direction and that the vector lies in the semi-plane $\theta = \theta_0$ (without loss of generality we assume $\theta_0 = 0$). Let Ω_z and Ω_r be the components of the rotation vector in the axial and in the radial directions, respectively, for which we have: $\Omega_z = \Omega \cos\varepsilon$, $\Omega_r = \Omega \cos\theta \sin\varepsilon$. If ε is small these relations are simplified to

$$\Omega_z \simeq \Omega \quad \text{and} \quad \Omega_r \simeq \varepsilon\Omega \cos\theta \tag{4.4}$$

and this means that the effect of the axial rotation remains essentially unchanged while an asymmetric radial forcing is introduced. The fact that the term Ω_r has a $\cos\theta$ azimuthal dependence means that an initially identical motion in the planes $\theta = 0$ and $\theta = \pi$ will be subject to Coriolis forces due to Ω_r identical in magnitude

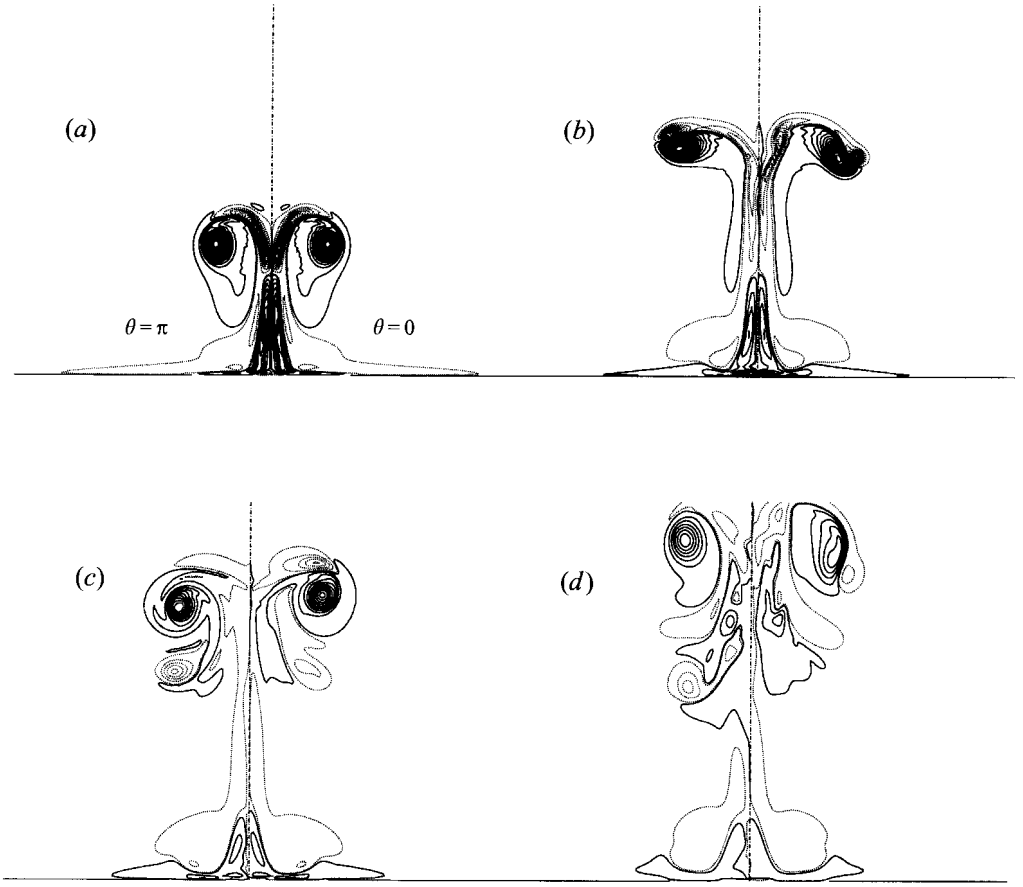

FIGURE 18. Contour plot of azimuthal vorticity for a vortex ring at $Re = 1500$ and $Ro = 10$: (*a*) $t = 7.26$, (*b*) $t = 14.5$, (*c*) $t = 21.8$, (*d*) $t = 29$. The initial angle of inclination between the direction of propagation and the rotation vector is 3°. The straight dotted lines show the direction orthogonal to the orifice. Vorticity increments $\Delta\omega = \pm 0.4$.

but opposite in direction; therefore an asymmetry is most likely to occur. Direct inspection of the phenomenon by numerical simulation has shown that it was indeed the case. Consistent with the flow visualizations, an initial small misalignment of only 3°, has a large effect on the flow as shown in figure 18, which shows results from the three-dimensional numerical simulation.

5. Conclusions

The main aim of the present paper has been to study the effects induced by background rotation on the dynamics of vortex rings. This vortex structure is in fact relatively simple and controllable; therefore its study can be pursued in detail. Nevertheless, the vortex ring dynamics is rich with interesting features pertaining to more complex flows, like round jets and swirling flows in combustion chambers, and can be thought of as a building block for such flows.

The analysis has been performed by numerical and laboratory experiments, using the two methodologies as complementary tools. Results have shown that for low rotation rates $Ro \gtrsim 3$ the vortex ring is slowed down by the rotation and an oppositely signed structure forms in front of the ring. For low Reynolds numbers

($Re \simeq 500$) these structures diffuse one into another and the peak vorticity in the ring undergoes a rapid decrease. For higher Reynolds numbers ($Re > 1000$) part of the diffusion is prevented and the primary ring turns out to be strong enough to elongate the oppositely signed vorticity in a thin layer. This layer, being unstable, rolls up to form a secondary vortex ring that propagates in a direction opposite to the primary ring.

Some of the phenomena described for this rotation regime have been observed also by Virk *et al.* (1994) in vortex rings without background rotation but with an assigned swirling flow. This is not surprising, because in their experiments the swirl was not confined to the core of the ring, but it extended to a larger flow region. The same arguments applied to understand our results could therefore be used in the interpretation of their experiments.

For higher rotation rates the scenario changes. In particular, as the thin vorticity layer released from the orifice edge starts the roll-up process, intense oppositely signed vorticity is generated due to rotation. This implies that strong cross-cancellation has acted since the beginning, thus preventing the vortex ring from forming. At the same time, oblique shear layers of large axial extent are generated and they have been identified as features of inertial waves. Owing to the transient nature of the forcing, many frequencies are excited and this usually results in a band of angles γ between the wave patterns and the axis of symmetry. Also, the angle γ decreased in time, but, for a fixed time the dependence of γ on the Rossby number was well described by the relation $\gamma = \sin^{-1}(Rof)$, f being the excitation frequency.

The limit $Ro \approx 3$ between high- and low-rotation regimes has been fixed in this study by the observation that for $Ro < 3$ the peak azimuthal vorticity was no longer located in the core of the ring for the whole evolution. We wish to stress that this criterion is subjective and has been used mostly for ease of presentation of the results. In the experiments we have observed that there is a range of Rossby numbers where different phenomena belonging to the two regimes coexist and the flow dynamics is a combination of both.

Finally we would like to mention that in some laboratory experiments the ring was observed to develop an asymmetry, which led one side of the ring to evolve faster than the other. This yielded a ring inclined at a certain angle with respect to the axis of rotation. For high Reynolds numbers ($Re \simeq 1000$) the inclination amplified in time and the flow degenerated to a fully three-dimensional configuration. Three-dimensional numerical simulations of the phenomenon have shown that the reason for this loss of symmetry was a small initial misalignment between the axis of rotation and the direction of translation. The systematic study of this mechanism, however, will be the subject of a future paper.

Before concluding, we wish to emphasize that we concentrated only on the case where the swirl was self-generated by the flow dynamics. Different kinds of swirl, for example supported only in the vortex core, could also be considered and they may have quite different properties from the one considered in this paper. The interest in these structures, however, would be mostly theoretical, since it is almost impossible to generate such vortices experimentally and therefore they are not likely to be found in real applications.

R.V. and P.O. acknowledge the support by a grant MURST 60% (Ministero dell'Università e della Ricerca Scientifica e Tecnologica). G.F.C. acknowleges support from the Office of Naval Research (Number N00014-96-1-0065), the National Science Foundation (OCE 91-21998) and the San Diego Supercomputer Center.

REFERENCES

ABRAMOWITZ, M. & STEGUN, I. A. 1964 *Handbook of Mathematical functions with Formulas, Graphs and Mathematical Tables.* National Bureau of Standards.

AYOTTE, B. A. & FERNANDO, H. J. S. 1994 The motion of a turbulent thermal in the presence of background rotation. *J. Atmos. Sci.* **51**, 1989–1994.

DALZIEL, S. 1992 *DigImage. Image Processing for Fluid Dynamics.* Cambridge Environmental Research Consultants Ltd.

GREENSPAN, H. P. 1968 *The Theory of Rotating Fluids.* Cambridge University Press.

HELMHOLTZ, H. 1858 On integrals of the hydrodynamical equations which express vortex motion. Translation by P. G. Tait in *Phil. Mag.* **33**(4), 1867, 485–512 .

KELVIN, LORD (THOMSON, W.) 1867 A letter in the appendix to Helmholtz (1858) in the translation of P.G. Tait.

MÉTAIS, O., FLORES, C., YANASE, S., RILEY, J. J. & LESIEUR, M. 1995 Rotating free-shear flows. Part 2. Numerical simulations. *J. Fluid Mech.* **293**, 47–80.

MOFFATT, H. K. 1988 Generalized vortex rings with and without swirl. *Fluid Dyn. Res.* **3**, 22–30.

ORLANDI, P. & VERZICCO, R. 1993 Free vortex rings, analogies and differences between vorticity and passive scalar, In *Vortex Flows and Related Numerical Methods*, (ed. J.T. Beatle *et al.*) Kluwer.

SAFFMAN P. G. 1975 On the formation of a vortex ring. *Stud Appl. Maths* **54**, 261–268.

SAFFMAN P. G. 1978 The number of waves on unstable vortex ring. *J. Fluid Mech.* **84**, 625–639.

SALLET, D. W. & WIDMAYER, R, S. 1974 An experimental investigation of laminar and turbulent vortex rings in air. *Z. Flugwiss.* **22**, 207–215.

SHARIFF, K., VERZICCO, R. & ORLANDI, P. 1994 A numerical study of three-dimensional vortex ring instabilities: viscous corrections and early non-linear stages *J. Fluid Mech.* **279**, 351–375.

STEVENSON, T. N. 1973 The phase configuration of internal waves around a body moving in a density stratified fluid. *J. Fluid Mech.* **60**, 759–767.

THOMSON, W. 1867 On vortex atoms. *Phil. Mag.* **34**(4), 15–24.

TRITTON, D. J. 1992 Stabilization and destabilization of turbulent shear flow in a rotating fluid. *J. Fluid Mech.* **241**, 503–523.

TURKINGTON, B. 1989 Vortex rings with swirl: axisymmetric solutions of the Euler equations with nonzero helicity. *SIAM J. Math. Anal.* **20**, 57–73.

VERZICCO, R., JIMÉNEZ, J. & ORLANDI, P. 1995 On steady columnar vortices under local compression. *J. Fluid Mech.* **299**, 367–388.

VERZICCO, R. & ORLANDI, P. 1995 Mixedness in the formation of a vortex ring. *Phys. Fluids* **7**, 1513–1515.

VERZICCO, R. & ORLANDI, P. 1996 A finite–difference scheme for three–dimensional incompressible flows in cylindrical coordinates. *J. Comput. Phys.* **123**, 402–414.

VIRK, D., MELANDER, M. V. & HUSSAIN, F. 1994 Dynamics of a polarized vortex ring. *J. Fluid Mech.* **260**, 23–55.